Journal of Materials Chemistry A

ROYAL SOCIETY OF CHEMISTRY

PAPER

View Article Online
View Journal | View Issue

Cite this: J. Mater. Chem. A, 2026, 14, 11018

Exploring the potential of transition metal tungstates for photoelectrochemical water oxidation: a combined experimental and computational approach

Ana Caravaca, Francisco J. Pastor, Andrés Parra-Puerto,* Nathalia C. Verissimo, Néstor Guijarro, Teresa Lana-Villarreal and Roberto Gómez*

The combination of experimental and computational methodologies offers a reliable strategy to not only discover new materials but also rationalize their performance and their intrinsic limitations. Following this concept, fourth-period metal tungstates (RWO_4, R = Mn, Fe, Co, Ni, Cu or Zn) have been explored for their application as photoanodes for solar water oxidation. The theoretical screening of these materials reveals large effective masses for both electron and hole carriers, while the density of states (DOS) profiles indicate that only Fe and Cu tungstates show adequate features to be photoanodes. This agrees with experimental data showing that they yield the best photocurrents in the series. In fact, $FeWO_4$ reaches over 0.04 mA cm^{-2} at 1.23 V_{RHE} under one sun, a value 67% higher than the current record. The still low photoactivity is partly linked to the fact that the electrode deviates from the band edge pinning regime over a wide potential range. Under the same conditions, $CuWO_4$ delivers a photocurrent over 0.3 mA cm^{-2}, in line with the best results found in the literature. Overall, the exploratory analysis performed in this paper not only identifies the parameters that limit the photoelectrochemical response of a wide range of metal tungstates, but it enables the identification of iron and copper tungstates as promising photoanodes for solar water oxidation whose performance may be enhanced by the implementation of some modification strategies.

Received 6th October 2025
Accepted 2nd February 2026

DOI: 10.1039/d5ta08157b

rsc.li/materials-a

1 Introduction

Photoelectrochemical (PEC) cells can perform water electrolysis by using sunlight, generating hydrogen with low or ideally zero applied bias. Such unassisted water splitting can be more easily achieved by employing a dual-absorber tandem cell configuration, which involves the assembly of a photoanode and a photocathode (generating hydrogen and oxygen, respectively).[1] However, current semiconductor electrodes show several limitations. In the case of photoanodes, they tend to have a rather high onset potential, low photocurrents, and relatively poor chemical stability.[2] In the course of the last decades, there have appeared several studies addressing semiconductor composition and synthesis routes oriented to overcome these limitations.[3–5] An ideal photoanode must possess some characteristics such as (a) efficient solar light harvesting (band gap around 2.0 eV for a single-photoelectrode device); (b) long-term stability against photocorrosion; (c) low electron–hole recombination (favored by highly mobile carriers and fast electron–hole separation), and (d) efficient hole transfer to water/hydroxide at the electrode/electrolyte interface. Unfortunately, no material has yet been found that satisfactorily fulfils all the requirements to sustain efficient water photooxidation.[6]

In the past years, simple oxides based on earth-abundant materials (*i.e.*, α-Fe_2O_3,[7] WO_3,[8] or TiO_2 [9]) have been extensively studied due to their scalable synthesis routes and acceptable photoresponse, with photocurrent densities achieving up to 6.5 mA cm^{-2}.[10] In this respect, numerous studies have focused on tungsten trioxide,[8] as it presents a band gap ranging between 2.6 to 3 eV,[11,12] moderate hole diffusion length (around 150 nm) and high electron mobility (μ_e = 12 cm^2 V^{-1} s^{-1}) compared to hematite and titanium dioxide,[13,14] high chemical stability in acid media,[15] and suitable band edge positions to drive the water oxidation reaction.[16] Also, tungsten is a relatively abundant[17] and cost-effective element, which makes it a good candidate to put research effort into improving the activity of tungsten trioxide. However, WO_3 is not stable against photocorrosion in alkaline media,[18] and it presents weak light absorption in the visible range (α = 10^4–10^5 cm^{-1}).[19] Thus, several alternatives are emerging to address these issues and

Departament de Química Física i Institut Universitari d'Electroquímica, Universitat d'Alacant, Apartat 99, E-03080 Alicante, Spain. E-mail: roberto.gomez@ua.es; andres.parra@ua.es

enhance the oxide properties. One of the most prominent is the use of related ternary oxides, such as metal tungstates, due to their potentially more favorable band gap and enhanced stability, especially in neutral to basic media (pH above 4).

The metal tungstate most widely reported as a photoelectrode is $CuWO_4$, with a band gap between 2.2 to 2.4 eV, high chemical stability, and the ability to carry out the photooxidation of water. However, its photocurrent is usually affected by fast electron–hole recombination. Several strategies have been explored to address this issue.[20–22] For instance, Yang *et al.* and Ikeue *et al.* reported that Mo doping effectively narrows the band gap and increases the electron carrier density.[23,24] The construction of heterojunctions to suppress charge-carrier recombination has also been widely used; WO_3 has frequently been employed as an underlayer[25–27] or as a part of local heterojunctions.[28] Other studies have introduced $NiWO_4$, CdS, and $BiVO_4$ underlayers.[29–31] Surface charge-separation efficiency has additionally been improved through the incorporation of cocatalysts, such as Co–Pi, and Ni–Pi.[32–34] Furthermore, collection efficiency has been enhanced by tailoring the nanostructure of $CuWO_4$.[35] Some studies have also appeared on the potential use as photoanodes of other metal tungstates, such as $FeWO_4$,[36] $SnWO_4$,[37] $MnWO_4$,[38] $CoWO_4$,[39] and $NiWO_4$.[40]

Density Functional Theory (DFT) stands out as a reliable methodology to better understand these materials, predicting both properties and potential drawbacks. This should lead to a more efficient design and optimization of the materials studied. In the literature, one can find DFT calculations for the previously mentioned tungstates,[41–43] although it is rare to find a theoretical screening of these materials.[44,45] In most cases hybrid functionals or the Hubbard correction have been applied to increase accuracy because the method of the Generalized Gradient Approximations (GGA) functional parametrized by Perdew, Burke, and Ernzerhof (PBE) tends to underestimate semiconductor band gaps.[46] Most of these studies focus on fundamental aspects and photocatalytic applications, with only a few of them dealing with photoelectrochemical aspects.[47–49]

This work focuses on the investigation of a series of metal tungstates, RWO_4 (R = Mn, Fe, Co, Ni, Cu, and Zn) synthesized following the same sol–gel procedure. Subsequent theoretical screening provides their electronic structure, including the carrier effective masses, and their band gap values and types. Such computational output enables both rationalizing the experimental results and gaining further physical insights. It is shown how, by combining theory and experiment, the possible drawbacks for these materials are more easily tracked and tackled in an effective way. As an outcome of this study, $FeWO_4$ and $CuWO_4$ are identified as the most promising materials for water splitting photoanodes. Overall, this study shows how tungstates may be used instead of tungsten trioxide, particularly once methods for enhancing carrier mobility are found and implemented.

2 Experimental

2.1 Materials preparation

The materials were synthesized following a sol–gel-based spin coating method.[33] Briefly, 0.685 mmol of citric acid are dissolved in 2.5 mL deionized water and 1.25 mL 2-methoxyethanol. Then, 3.746 mmol of the divalent cation precursor (R = Mn^{2+}, Fe^{2+}, Co^{2+}, Ni^{2+}, Cu^{2+} and Zn^{2+}) are added. Once the previous solution is completely homogenized, 0.312 mmol of ammonium metatungstate (AMT) are introduced (Fig. S1). F:SnO_2-coated glass (FTO, Pilkington TEC15) is cleaned by immersion for 5 min in soapy water and for another 5 min in deionized water and then dried in air at ambient temperature. Next, 25 μL of the precursor solution are dropped on a 1 cm^2 FTO piece and spin-coated at 1500 rpm for 30 s. The number of layers applied according to this procedure was optimized for both $CuWO_4$ and $FeWO_4$, which revealed that using 8 layers yields the highest photocurrent (Fig. S2). Each layer was pretreated for 8 min at 350 °C in an oven prior to the application of subsequent layers. Unless otherwise stated, all the samples are made of 8 layers. The final film was thermally treated at 500 °C for 3 hours (ramp rate of 3 °C min^{-1}).

2.2 Materials characterization

X-ray diffraction (XRD) experiments were carried out using a Bruker Advance D8 with Cu-Kα radiation (λ = 1.5418 Å) generated at 40 kV and 40 mA. Experiments scanned 2θ from 10° to 45° with 0.02° per step. A Shimadzu UV-3600i Plus spectrophotometer with an integrating sphere working in absorbance mode was used for the optical properties. The top-view film morphology was obtained by scanning electron microscopy (SEM) (Jeol IT500HR/LA instrument at an acceleration voltage of 10/15 KV). Furthermore, an energy dispersive X-ray spectrometer (EDS) was employed to analyze the sample surface chemical composition.

2.3 Electrochemical characterization

Photoelectrochemical measurements were carried out at room temperature in a three-electrode cappuccino-type cell equipped with a quartz window by using a potentiostat-galvanostat (Autolab, PGSTAT30). An Ag/AgCl/KCl (3 M) was used as a reference electrode (all the potentials converted to the reversible hydrogen electrode, RHE), and an Au wire as a counter electrode. A 0.2 M potassium phosphate (KPi) buffer (pH 7), a 0.1 M potassium borate (KBi) buffer (pH 9), and solutions 0.1 M KOH, 0.1 M H_2SO_4 were used as working electrolytes. All the experiments were conducted under substrate-electrode (SE) illumination, unless stated otherwise, with an intensity of 0.1 W cm^{-2} (1 sun) delivered by a solar simulator (SAN-EI ELECTRONIC) equipped with an AM 1.5 G filter. An ozone-free 1000 W Xe (Hg) arc lamp (Newport Instruments) was also used together with a UV filter (Newport model FSQ-KG3, λ > 350 nm) for some measurements with $FeWO_4$ and $CuWO_4$ electrodes. Incident photon to current efficiency (IPCE) was measured using a Xe arc lamp (Newport 66 902, Thermo Oriel) together with a monochromator (Cornerstone 260, Oriel Instruments). Measurements were taken every 10 nm in the wavelength range from 600 to 300 nm while keeping the electrode potential at 1.23 V. An optical power meter (model 70 310 from Thermo Oriel) and a photodiode (model 71 638, Thermo Oriel) were used to measure the light power at each wavelength.

Mott–Schottky (MS) plots were obtained by performing Electrochemical Impedance Spectroscopy (EIS) measurements at frequencies ranging from 10^5 Hz to 0.1 Hz with an amplitude of 10 mV and at applied potentials from 0.74 to 1.64 V_{RHE}.

2.4 DFT calculations

DFT calculations were carried out using the Vienna *Ab Initio* Simulation Package (VASP)[50] with the Projector Augmented Wave (PAW) method[51,52] at the PBE + *U* level (employing the Dudarev[53] approach). Using this approach an accurate band gap value cannot be obtained as it leads to significant DOS distortion (due to high *U* values). In our work, we have prioritized obtaining reliable DOS profiles. All calculations were performed following the work done by Pastor *et al.*[54] To sum up, the plane-wave energy cutoff was 520 eV, and spin-polarized calculations were performed by arranging the magnetic moments in antiferromagnetic and ferromagnetic configurations and selecting that with the lowest energy. In all cases, such a configuration was the antiferromagnetic arrangement. As a particular case, $ZnWO_4$ was considered as diamagnetic.[55–61] The U_{eff} values (Table S1) were selected from the bibliography.[29,43,50] The structures were obtained from the Crystallography Open Database (COD). All the tungstates present a monoclinic structure (*P*12/*c*1) except for $CuWO_4$, which is triclinic (–*P*1).

3 Results and discussion

3.1 Theoretical results

DFT calculations were carried out for the family of oxides RWO_4 with R = Mn, Fe, Co, Ni, Cu, and Zn. Fig. 1 shows the profiles for the density of states (DOS) calculated at the PBE + *U* level for all the structures adopting the *U* values given in Table S1.

The DOS for the valence bands (VBs) (depicted on the left of each panel of Fig. 1) are formed by O_{2p} states hybridized with other states of the two transition metals. Likewise, the DOS corresponding to the conduction bands (CBs) (displayed on the right) show a prominent contribution of W_{5d} levels, except for $CuWO_4$. The band gap (E_g) is defined by R_{3d} states near the edges of the bands for most tungstates (except for $NiWO_4$ and $ZnWO_4$). In any case, the DOS for these compounds and that for tungsten tioxide[62] show some common characteristics as the VBs are mainly constituted by O_{2p} states, whereas the CBs are composed of W_{5d} states. The Mn, Fe and Co tungstates show a localized R_{3d} contribution in the upper part of the VB, while $CuWO_4$ shows Cu_{3d} localized states in the lower part of the CB, suggesting the prevalence of hopping-type conductivity. These localized states are associated with the VB and the CB, respectively.

The tungstates can be classified according to their DOS into three different types: (i) $MnWO_4$, $FeWO_4$, and $CoWO_4$ type: it shows localized R_{3d} states just below the Fermi level, which may act as hole traps. Moreover, Mn and Fe tungstates present W states in the CB, which suggests that the photogenerated carriers would be in different atoms. In contrast, $CoWO_4$ also shows R_{3d} states in the CB and thus the photogenerated carriers would not necessarily be spatially separated, which could favor recombination. (ii) $NiWO_4$ and $ZnWO_4$ type: it is characterized by a large value of E_g, as defined by O states in the VB and W states in the CB. (iii) $CuWO_4$ type: it presents R_{3d} localized states associated with the CB, and oxygen states in the VB. The R_{3d} states of $CuWO_4$ would be characterized by a low degree of hybridization with the rest of the atoms in the crystal structure and they may act as electron traps. Tian *et al.* have reported the DOS for $CuWO_4$ as obtained *via* XPS VB and O K-edge XAS.[47] It is worth noting that it aligns well with the total DOS derived here from DFT. In addition, the XPS VB spectra for iron tungstate[63,64] and cobalt tungstate[63] show the prevalence of R_{3d} states, as shown in Fig. 1b and c. These results are consistent with previously reported data for Co and Zn tungstates.[65,66]

Fig. 2 presents the band structure obtained for each RWO_4 at the PBE + *U* level, while Fig. 3 shows the calculated effective masses for the charge carriers, which are key to understanding

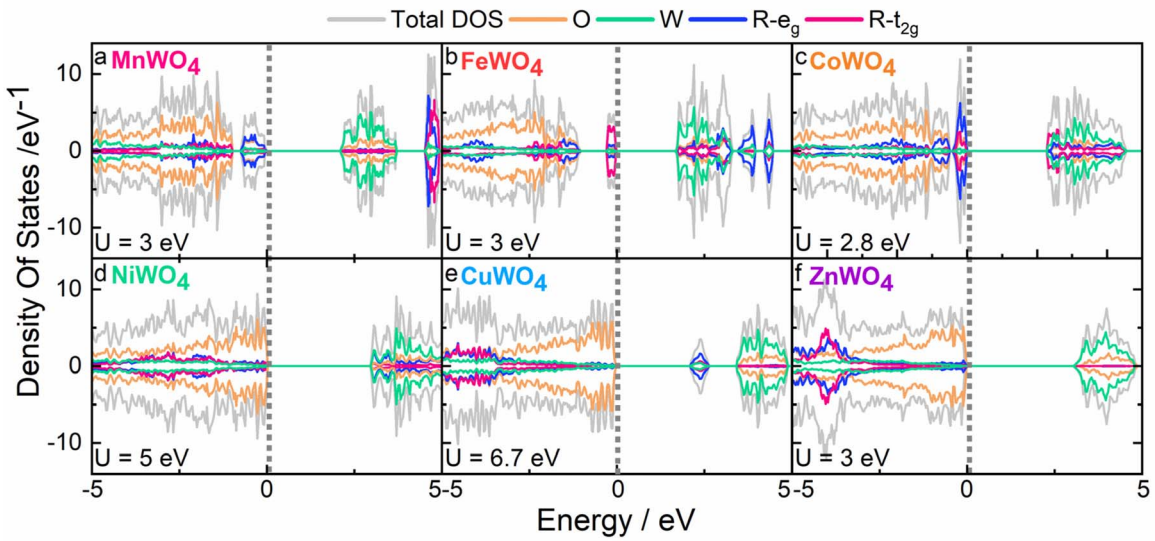

Fig. 1 DOS profiles for (a) $MnWO_4$, (b) $FeWO_4$, (c) $CoWO_4$, (d) $NiWO_4$, (e) $CuWO_4$ and (f) $ZnWO_4$, calculated at the PBE + *U* level. The *U* values are indicated in each panel. The Fermi level is set at 0 eV (dotted grey line).

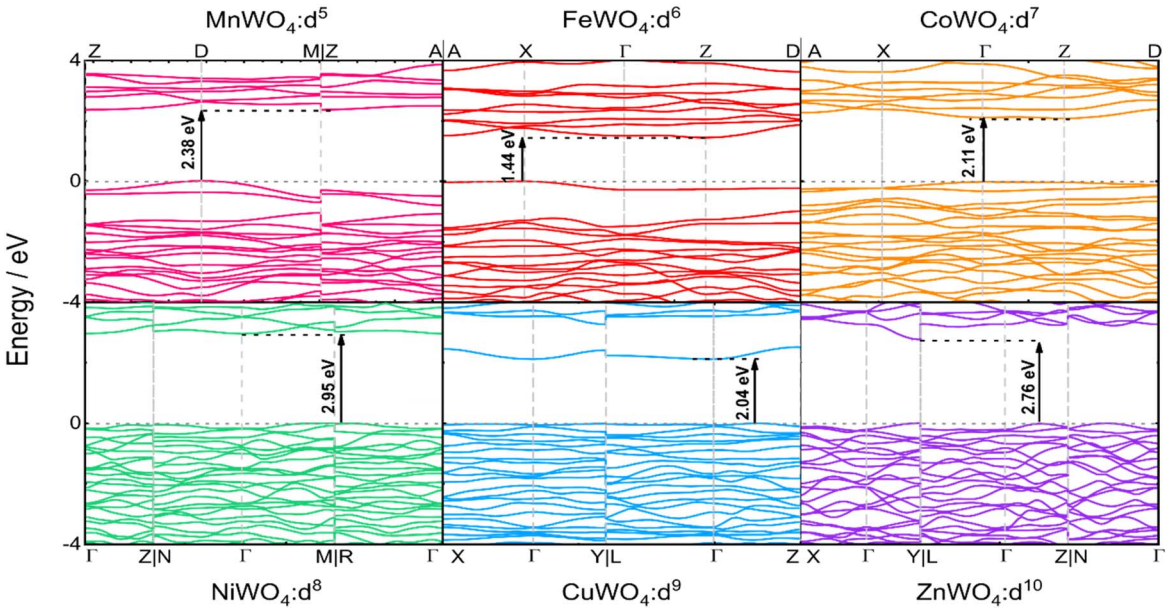

Fig. 2 Band structures for the RWO_4 tungstates at the PBE + U level.

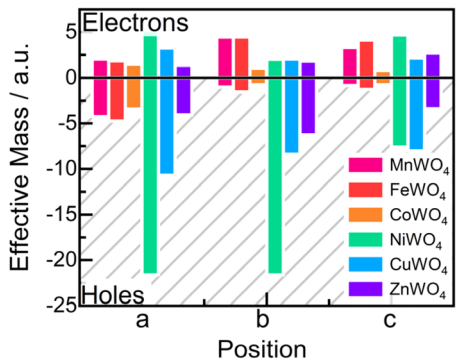

Fig. 3 Schematic representation of the carrier effective masses obtained for the fundamental E_g (with the Boltztrap2 model) for the RWO_4 tungstates at the PBE + U level (a, b, and c correspond to the vectors defining the unit cell).

the limitations of these materials. From Fig. 2, both CB and VB edges are shown to be characterized by a low curvature, which indicates low charge carrier mobility and weak hybridization in the structure.[67] Moreover, all samples present an indirect E_g as shown in Fig. 2 and Table S2. Results in Fig. 3 suggest that Mn, Fe, and Co tungstates exhibit rather anisotropic electric conduction, as their electron and hole effective masses vary significantly along the *a*, *b* and *c* directions. In contrast, Ni, Cu, and Zn tungstates show a more isotropic behavior, with effective masses that are relatively similar along the main directions. Furthermore, the relative magnitudes of electron and hole effective masses ($m_e^* < m_h^*$) for Ni, Cu, and Zn tungstates indicate a tendency toward n-type conductivity.

3.2 Experimental results

3.2.1 Physical characterization. The same sol–gel synthesis[33] route was used for preparing all the materials to develop a consistent experimental benchmarking. The precursor solutions are based on metal nitrates (although $FeCl_2$ was used for iron), which could impact the photoelectrode behavior.[68]

With the aim to study the particle nature, the RWO_4 samples were analyzed in terms of particle size, composition, and elemental distribution by means of Scanning Electron Microscopy (SEM) and Energy Dispersive Spectroscopy (EDS) (Fig. 4, and S3–S5). The morphology of the layer is important as it may play a role in determining the electron–hole recombination rate.[69] The sol–gel method normally yields rather compact thin films composed of nano- or microparticles. The top-view images of the $MnWO_4$, $CoWO_4$ and $ZnWO_4$ thin films (Fig. 4a, c and f, respectively) reveal a morphology composed of agglomerated small particles, yielding a smooth surface. In the case of $NiWO_4$ (Fig. 4d), some larger spherical particles also appear on top of the smooth layer. On the other hand, $FeWO_4$ (Fig. 4b) displays larger particles, while $CuWO_4$ (Fig. 4e) exhibits a more defined morphology consisting of spherical particles and some flakes.

The thickness of the different electrodes was measured from cross-sectional images (insets in Fig. 4). The thickness values estimated for each electrode are 3.0 μm ($MnWO_4$), 2.6 μm ($FeWO_4$), 2.5 μm ($CoWO_4$), 3.2 μm ($NiWO_4$), 1.2 μm ($CuWO_4$), and 1.6 μm ($ZnWO_4$). The differences observed in thickness values may be due to the role of metal ions in the sol–gel process,[70] which may impact the viscosity of the solution and thus the final thickness of the spin-coated samples. Elemental mapping using EDS is shown in Fig. S5(a–f). All the samples show a homogeneous compositional distribution.

3.2.2 Theoretical and experimental band diagrams for RWO_4 tungstates. XRD patterns were obtained for both thin films (Fig. 5) and powders (Fig. S6). The thin film XRD patterns for $MnWO_4$, $FeWO_4$, $CoWO_4$, $NiWO_4$ and $ZnWO_4$ display the (100), (011), (110), and (111) peaks characteristic of the

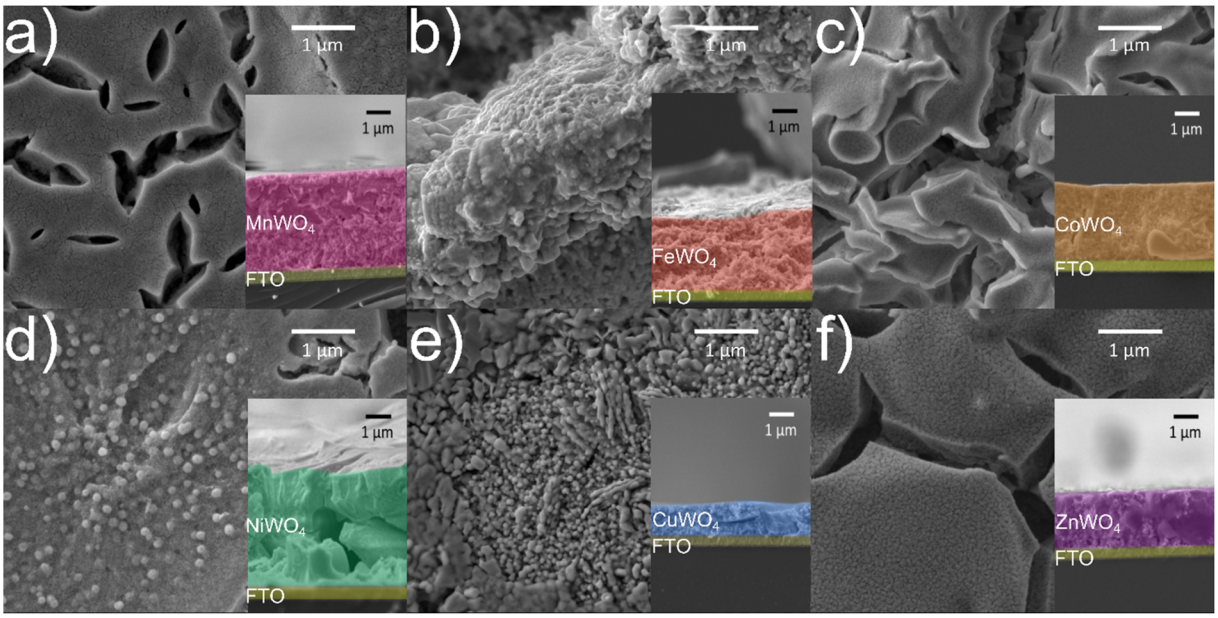

Fig. 4 SEM top-view and cross-section (inset) images for (a) Mn, (b) Fe, (c) Co, (d) Ni, (e) Cu and (f) Zn tungstate films annealed at 500 °C for 3 h. The colored portions of the cross-section highlight the sample thickness, while the yellow portion indicates the thickness of the FTO film.

monoclinic crystalline structure ($P2/c$ space group, COD no: 00-152-0200, 00-900-8124, 00-810-3677, 00-810-3678 and 00-2110-1674) at $2\theta = 18.4$, 23.5, 24 and 30°, respectively. On the other hand, the $CuWO_4$ sample shows the (010), (100), (110), (01−1), (011), (10−1), (11−1), (111), (020), (1−1−1) and (1−11) peaks typical of the triclinic crystalline structure ($P\bar{1}$ space group, COD no: 00-100-8036) at $2\theta = 15.3$, 19.0, 22.9, 23.6, 24.1, 25.9, 28.7, 30.2, 30.8, 31.6 and 32.2°, respectively. The peaks observed for thin films (Fig. 5 and S7) are the same as for the powders (Fig. S6). However, for the $FeWO_4$ powder, there appear weak WO_3 peaks, which are not shown in the thin film (Fig. 5). In any case, some electrochemical measurements were carried out to verify the absence of significant amounts of surface WO_3 in the $FeWO_4$ thin film (Fig. S8).

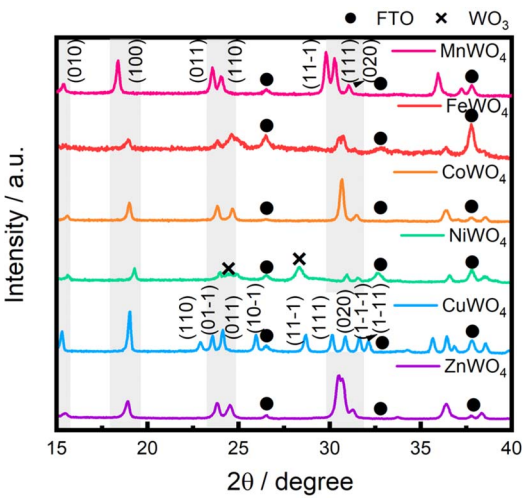

Fig. 5 XRD patterns for the different tungstates (as thin films) prepared by sol gel; × → WO_3 and ● → FTO (database standard reference information for the XRD patterns are shown in Fig. S7).

Once confirmed that the desired materials were synthesized, the experimental values of E_g were determined from UV-vis spectra (Fig. 6a) by means of Tauc plots, both for direct, E_g^{Dir} (Fig. 6b) and indirect transitions, E_g^{In} (Fig. 6c). As shown in Fig. 6a, $CoWO_4$ presents a secondary absorption band in the range from 640 nm to 500 nm (corresponding to the bluish color of the sample), together with the main absorption below 450 nm. $NiWO_4$ also presents a secondary absorption band at ~430 nm. Such bands are due to spin-allowed transitions for the Co^{2+} and Ni^{2+} ions, which happen between the t_{2g} and e_g subshells.[54,71–73] A comparison of Fig. 1c and 6a firmly supports this assignment. The main feature in the spectra (below 450 nm) is ascribed to electronic excitations from O_{2p} to W_{5d} orbitals in the $[WO_4]^{2-}$ and $[WO_6]^{6-}$ groups.[71] The materials with the narrowest E_g within this family are $FeWO_4$ and $CuWO_4$, providing the best light harvesting efficiency, whereas Ni and Zn tungstates display a much wider E_g minimizing light harvesting. Table S4 shows a compilation of experimental and theoretical E_g values obtained in this work and from the literature. Both sets of values are quite similar.

3.2.3 Photoelectrochemical characterization. To gain insights into the band edge energies, flat band potentials (E_{fb}) were determined for all the tungstates (Fig. S9) *via* an MS analysis. Only $CuWO_4$ exhibits a well-defined MS plot for an n-type semiconductor electrode with a flat band potential of 0.5 V *vs.* RHE (Fig. S9e), indicating band edge pinning (BEP). MS plots were obtained both in the dark and under illumination (100 mW cm^{-2}, Fig. S10), being rather similar. On the other hand, OCP experiments were carried out under different light intensities (Fig. S11), yielding an E_{fb} value very close to that determined through MS plots and confirming the BEP regime. On

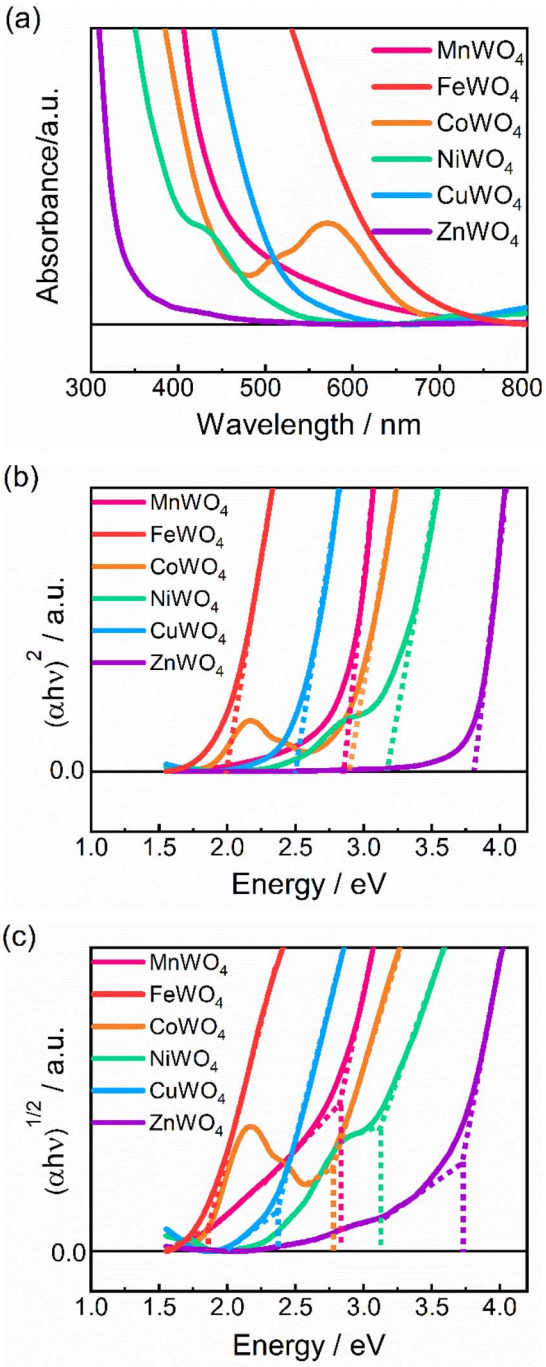

Fig. 6 (a) UV-vis absorption spectra and Tauc plots for direct (b) and indirect (c) band gaps (E_g^{Dir} and E_g^{In}) for RWO_4 thin films.

the other hand, $MnWO_4$ shows a MS plot typical of a p-type semiconductor under BEP. For the rest of the tungstates, atypical MS plots are obtained, suggesting partial band unpinning and even a behavior close to that of Fermi level pinning (FLP), which is likely due to the existence of a high density of surface states. Flat band potentials were thus estimated from the photocurrent onsets under chopped illumination as illustrated in Fig. S12.

The resulting E_{fb} values (0.5–0.7 V_{RHE} except for the case of the Mn tungstate) are similar or slightly higher than for other typical electrode materials reported in the literature, such as hematite[74] (E_{fb} between 0.4 to 0.8 V_{RHE}), bismurh vanadate[75,76] (E_{fb} between 0.1 to 0.68 V_{RHE}), or tin tungstate[77] (E_{fb} of about 0.32 V_{RHE}). To estimate the position of the CB edge, the flat band potential is assumed to be approximately equal to the potential corresponding to the CB edge. Thus, the following equations are used to estimate the value of the CB and VB edges:

$$\varepsilon_{CB}/eV \cong -4.44 - e(E_{fb}\ vs.\ SHE) \quad (1)$$

$$\varepsilon_{VB} = \varepsilon_{CB} - E_g \quad (2)$$

Fig. 7 gathers the locations of the band edges determined either theoretically or experimentally. The procedure followed for estimating the theoretical band edge positions is given in the SI.

As observed, the VB is lower in energy than the O_2/H_2O redox couple in all cases, which means that water photooxidation is thermodynamically feasible. Fig. 7 also shows that there are some localized electronic states in the Mn, Fe, and Cu tungstates (in agreement with theoretical calculations) that could be detrimental for their photoactivity as they may favor recombination. It is worth noting that experimental data do not exactly correspond to the expectations from the PBE + U calculations. These calculations are based on considering defect-free, bulk materials in contrast with real materials, with defects and, obviously, surfaces. Moreover, they tend to underestimate E_g values. In any case, there is an acceptable correlation between experimental and theoretical band edge positions (and thus between experimental and theoretical band gaps). This means that the calculations are able to capture the main trends.

To evaluate the photoelectrochemical response of these materials, linear sweep voltammograms (LSV) were recorded both in the dark and under illumination for electrodes with either similar (Fig. S13) or optimized thickness (Fig. 8a). The same trend is observed in both cases. $MnWO_4$, $CoWO_4$, $NiWO_4$ and $ZnWO_4$ (inset) show very modest photocurrents. In contrast, $FeWO_4$ delivers, for the optimal thickness, a significant photocurrent of 41 μA cm^{-2}@1.23 V_{RHE}, which represents a 64% increase over the state-of-the-art (Fig. 8b). $CuWO_4$ is the photoanode with the highest photoresponse, with 315 μA cm^{-2}@1.23 V_{RHE} for the optimized thickness, being this value (Fig. 8b) among the best reported in the literature.[78] Table S8 gathers relevant literature for different electrodes based on RWO_4 (from Mn to Zn).

It is worth noting that there is a relation between experimental and DFT results. The theoretical approach indicates that $CuWO_4$ and $FeWO_4$ are potential candidates as photoanodes because of their narrower E_g and their electronic state distribution, while the other materials could also be of interest. However, this needs to be and is clarified by means of experimental results, which show that only $FeWO_4$ and $CuWO_4$ yield significant photocurrents.

Only $FeWO_4$ and $CuWO_4$ can be considered as potential candidates for water photooxidation. Further analysis of their behavior was carried out for better understanding the charge carrier dynamics (mobility, effective masses, recombination…).

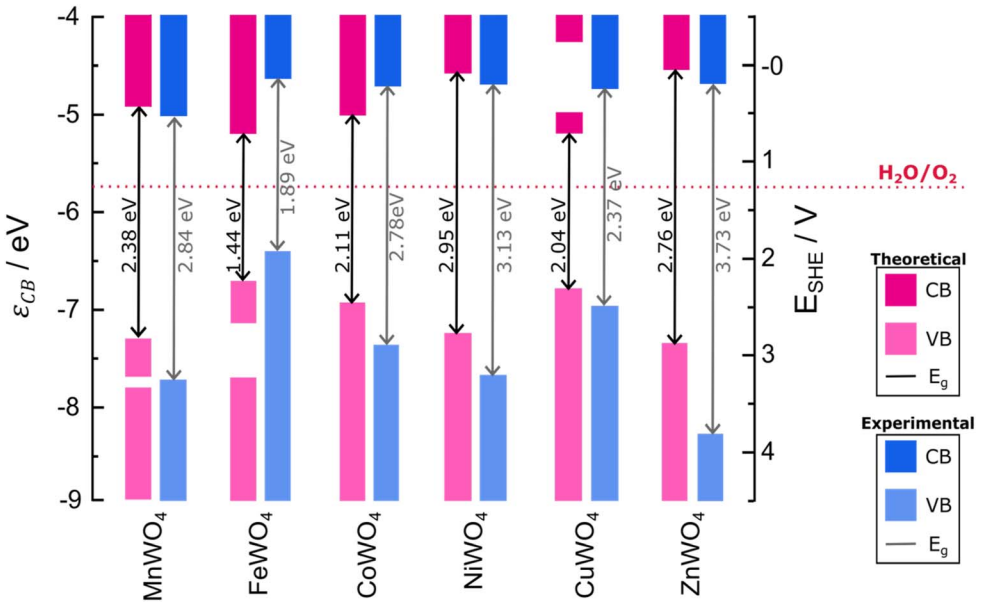

Fig. 7 Theoretical and experimental band diagrams for different RWO_4 tungstates.

This determines the maximum photocurrent that the material can achieve, and it may give hints on potential approaches to upgrade electrode performance. Experiments with more intense illumination (1 W cm^{-2}) were performed to assess the photocurrent response under increased photon flux (Fig. S14). The spectral distributions of the 1 W cm^{-2} and 0.1 W cm^{-2} sources differ. The 1 W cm^{-2} spectrum shows relevant peaks in the range of 275 to 325 nm, minimized using a UV filter. A ten-fold increase in the photoresponse is expected based on the illumination intensity difference, but the actual photocurrent enhancement is lower, as shown in Fig. S14a and b. The $FeWO_4$ electrode shows a photocurrent of 0.163 mA cm^{-2}@1.23V_{RHE} (4-fold increase relative to 1 sun), while the $CuWO_4$ electrode yielded 2.87 mA cm^{-2}@1.23V_{RHE} (9-fold increase). This fact can be attributed mainly to charge carrier recombination, together with some persisting differences in the spectral distribution of the illumination sources.

Both front illumination (Electrolyte-RWO_4-FTO, EE) and back illumination (FTO-RWO_4-Electrolyte, SE) were studied. Fig. S15 reveals higher photocurrents for SE illumination than for EE illumination for both $FeWO_4$ and $CuWO_4$. This is rather unexpected, and it shows that these electrodes have limitations derived from poor electron mobility and bulk recombination. In fact, back illumination diminishes the recombination probability.

Assessing the maximum attainable photocurrent requires the utilization of a hole scavenger such as methanol to mitigate surface recombination. Specifically, a 50% v/v ratio of methanol/electrolyte was used.[79] In such a medium, the catalytic efficiency is considered to be 100%, which means no surface recombination losses. Fig. 9a and b shows the photocurrent density in the presence (blue) and the absence (red) of methanol for both $FeWO_4$ and $CuWO_4$ electrodes. With the aim to get a straightforward overview of the materials limitations, the surface and bulk separation efficiencies (η_{surf} and η_{bulk}) have been determined and are shown in Fig. 9c. The potential-dependent charge separation efficiency at the semiconductor surface was determined according to:

$$\eta_{surf} = \frac{j_{Na_2SO_4}}{j_{MeOH}} \times 100 \quad (3)$$

where $j_{Na_2SO_4}$ is the photocurrent density (mA cm^{-2}) in the absence of hole scavenger, and j_{MeOH} is the photocurrent density in the presence of methanol (hole scavenger). The charge separation efficiency in the bulk was calculated according to:

$$\eta_{bulk} = \frac{j_{MeOH}}{j_{theo}} \times 100 \quad (4)$$

where j_{theo} is the theoretical absorption current density (13.2 mA cm^{-2} and 6.9 mA cm^{-2} for $FeWO_4$ and $CuWO_4$, respectively). Note that we have not considered the existence of current doubling for methanol photooxidation as it has been reported that it is not significant when the light intensity is around 1 sun or higher.[80]

Even though the η_{surf} values for these tungstates are high, around 73% ($FeWO_4$) and 65% ($CuWO_4$) at 1.23 V, η_{bulk} values are lower (around 0.24% for $FeWO_4$ and 6.6% for $CuWO_4$ at 1.23 V in both cases), being the $CuWO_4$ results in line with those in the literature.[81] They are also coherent with the high effective masses of the charge carriers and the existence of localized states as observed by DFT.[55] It can be seen that η_{bulk} increases at higher potentials for $CuWO_4$ likely due to a stronger band bending, which favors charge carrier separation and lowers charge recombination. In contrast, η_{bulk} for $FeWO_4$ does barely change with potential, as expected for electrodes that deviate from the BEP regime. $FeWO_4$ presents a much lower bulk efficiency compared with $CuWO_4$ (by 28 times), which can be further supported based on Fig. 1b, as $FeWO_4$ presents VB-

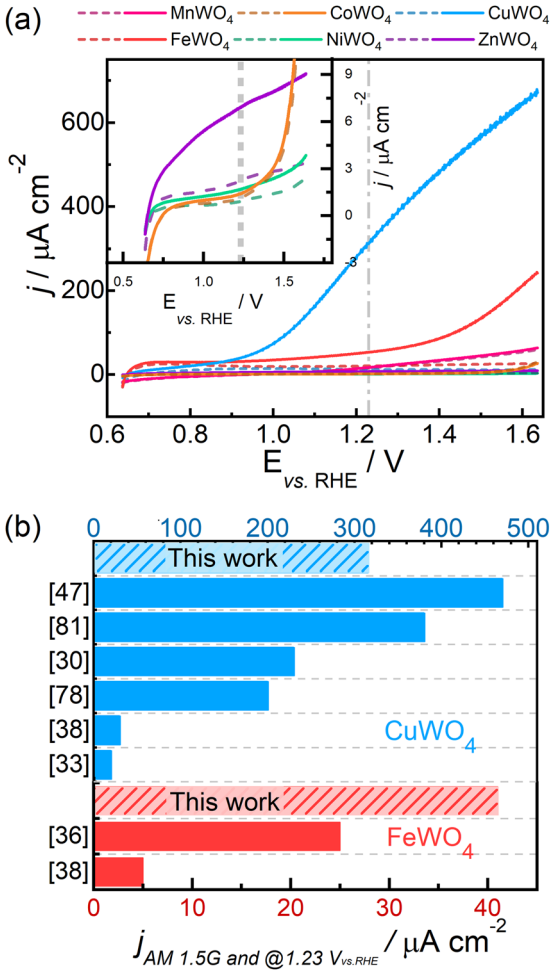

Fig. 8 (a) LSV for RWO_4 electrodes in phosphate buffer solution (pH 7) in the dark (dashed lines) and under 100 mW cm^{-2} SE illumination (solid lines). The curves for Ni, Zn and Co tungstates are given in the inset. (b) Values of j_{max}@1.23 V_{RHE} for $CuWO_4$ (blue, top) and $FeWO_4$ (red, bottom) for this work and in the literature.

associated Fe_{3d} localized states that may act as holes trap. For $CuWO_4$ the 3d localized states (less localized than for $FeWO_4$) are associated with the CB, acting in this case as electron traps (Fig. 1e), which is expected to have a lower impact as it affects the majority carriers.

The surface efficiency shows an unexpected behavior in the case of $FeWO_4$ as it decreases for increasing potentials above 1.1 V *vs.* RHE. Surface states seem to facilitate catalytic activity at low applied potentials, probably by mediating charge transfer, while under more oxidative conditions, they tend to behave as recombination centers. These results highlight the dual role of surface states in $FeWO_4$.

Recombination kinetics was also studied by means of photocurrent transients carried out at 1.23 V_{RHE} (Fig. 10a). When the light is on, a peak appears corresponding to surface accumulation of minority carriers, while a cathodic spike is observed upon turning off the light, resulting from the recombination of surface-trapped holes with FTO electrons. We define R as a normalized transient photocurrent density by means of eqn (5).[82–84]

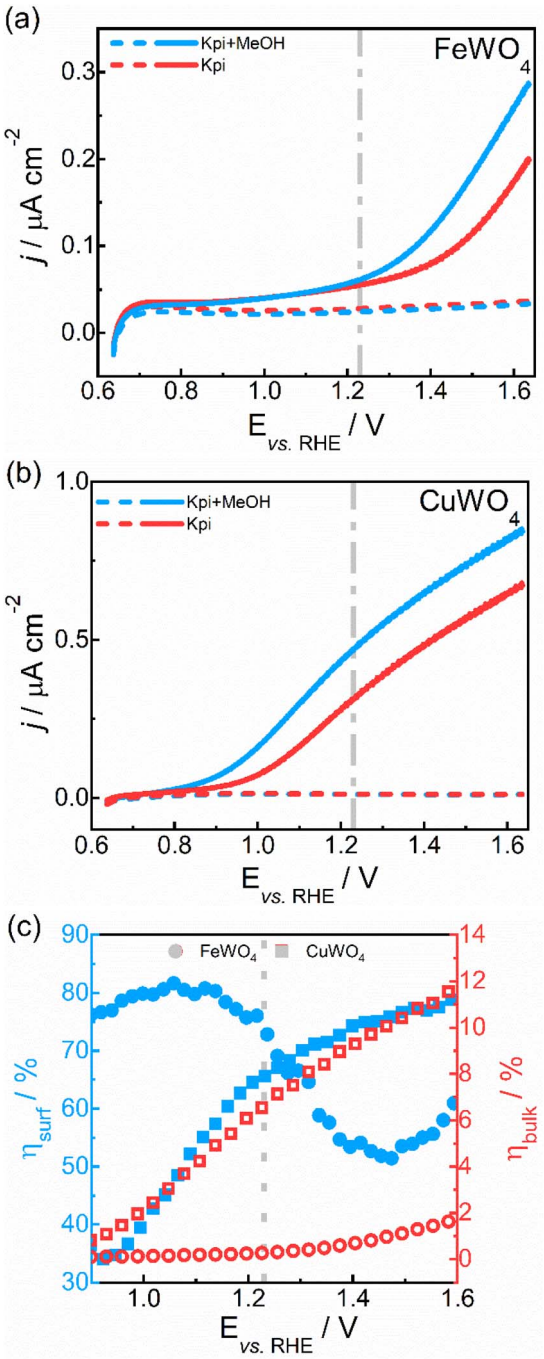

Fig. 9 LSVs for (a) $FeWO_4$ and (b) $CuWO_4$ with (blue) and without (red) 50% v/v ratio methanol as hole scavenger. The electrolyte was 0.1 M Na_2SO_4. Solid lines were obtained under illumination (100 mW cm^{-2}) while dashed lines were obtained in the dark. (c) Surface/bulk charge separation efficiencies (η_{surf}/η_{bulk}).

$$R = \frac{j_t - j_{st}}{j_{in} - j_{st}} \quad (5)$$

where j_t (mA cm^{-2}) is the time-dependent photocurrent density, j_{in} is the photocurrent density at time zero (light on) and j_{st} is the steady-state photocurrent density. To obtain a parameter giving information on the hole trapping kinetics at the electrode surface, the transient time constant (τ) is calculated as the time

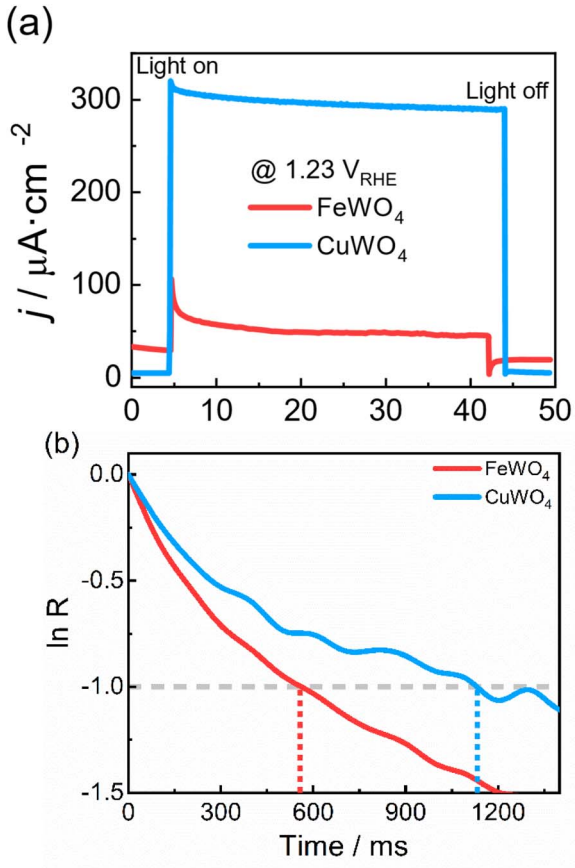

Fig. 10 (a) Photocurrent density–time curves of Fe and Cu tungstates measured under 1 sun illumination at 1.23 V_{RHE}. (b) Plot of ln R *vs.* time.

at which ln $R = -1$ (Fig. 10b). The values of τ are of 560 and 1130 ms for Fe and Cu tungstates, which indicates that holes get trapped faster at the $FeWO_4$ surface than at that of $CuWO_4$. In addition, electron lifetime (τ) was estimated for $CuWO_4$ from OCP decay measurements (Fig. S16). The resulting value of τ is relatively high (5 s), providing evidence of sluggish recombination kinetics.

Fig. 11 shows the incident photon to current efficiency (IPCE) as a function of wavelength for both $FeWO_4$ and $CuWO_4$ electrodes. $FeWO_4$ starts to show a photoresponse at around 600 nm, which indicates an effective E_g of about 2.1 eV, similar to the optical indirect E_g obtained through UV-vis measurements (Fig. 6b and c). $CuWO_4$ presents the onset at around 550 nm, corresponding to an effective E_g around 2.21 eV, which is comparable to the indirect E_g resulting from Fig. 6c. The integrated IPCE spectra (Fig. S17) yields a short-circuit photocurrent density (J_{SC}) of 44 μA cm^{-2} for $FeWO_4$ and 200 μA cm^{-2} for $CuWO_4$. The $FeWO_4$ value is almost identical to the photocurrent measured under simulated sunlight, whereas the value for $CuWO_4$ is 1.58 times lower. Such a difference likely indicates that the recombination processes are more sensitive to light intensity for $CuWO_4$ than for $FeWO_4$.

Finally, as the eventual enhancement of the stability of WO_3-related materials in a broad range of media was one of the motivations of this study, tungstates were tested in

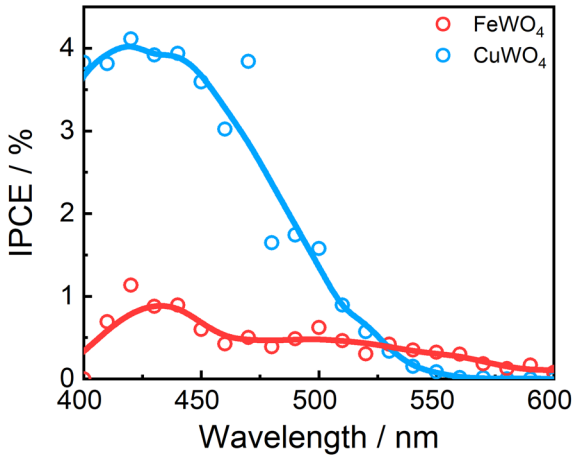

Fig. 11 Incident photon conversion efficiencies (IPCEs) under SE illumination.

solutions of different pH (pH values tested: 1, 7, 9 and 13.5) (Fig. S18a and b). The stabilities for $CuWO_4$ and $FeWO_4$ slightly depend on pH, with neutral media being more favorable. Relatively minor photocurrent decays of around 9% and 25% for $CuWO_4$ and $FeWO_4$, respectively, are though recorded after 3 h of continuous illumination. As in the case of WO_3, these materials are unstable in highly alkaline media (pH = 13.5–14).

From a practical perspective, sol–gel prepared Cu and Fe tungstates are promising transparent photoanodes due to their relatively narrow band gaps and good chemical stability. These features make them suitable for integration into tandem PEC devices in which they can be the front electrode (photoanode) to be combined with a second semiconductor electrode (photocathode) possessing a narrower band gap. These devices could potentially drive solar water-splitting without the application of a bias.[85,86] Further optimization through oxide modification, interface engineering, and optical management will be essential for designing efficient devices.

4 Conclusions

A series of transition metal tungstates (RWO_4; R = Mn to Zn) has been synthesized, characterized, and studied both experimentally (photoelectrochemical measurements) and theoretically (DFT). Calculations reveal that these tungstates can be divided into three categories according to the DOS profiles: (i) materials with R_{3d} states in the VB (Mn, Fe and Co tungstates); (ii) those with a wider band gap and no R_{3d} states near the band edges (Ni and Zn tungstates); and (iii) those with R_{3d} states associated with the CB ($CuWO_4$). The band diagrams show indirect E_g for all these materials, with relatively high values of the carrier effective masses. The theoretical results indicate that, out of the series, $CuWO_4$ and $FeWO_4$ are the most promising materials for photoelectrochemical applications despite the presence of d-states at the band edges, which may act as hole and electron traps. Specifically, for $FeWO_4$, minority carriers would be trapped at Fe_{3d} VB states, which can be hypothesized to have a significant impact on its

photoelectrochemical bulk efficiency. In the case of $CuWO_4$, the electronic structure points to the existence of electron traps, which are expected to affect to a lesser extent the electrode performance. UV-vis spectroscopy measurements confirm the indirect band gaps as well as the general trends theoretically predicted for the E_g values.

Mott–Schottky plots reveal that only $CuWO_4$ electrodes follow the BEP regime for an n-type semiconductor, which poses a limitation in the anodic photocurrents that the rest of the tungstates can deliver. Accordingly, an analysis of the photoelectrochemical performance for water oxidation reveals that the best performing material is $CuWO_4$, with a photocurrent over 0.3 mA cm^{-2}@1.23 V_{RHE} under 1 sun. $FeWO_4$ photoanodes yield a photocurrent over 0.04 mA cm^{-2}@1.23 V_{RHE}, which is relatively modest, but over 60% higher than the current state-of-the-art.

Although the photoresponses for the iron and copper tungstates are remarkable, these materials are still far from reaching their theoretical maximum photocurrents. This is a consequence of (i) the deviation from the BEP regime in the potential region of interest for $FeWO_4$ electrodes, (ii) the low bulk efficiencies due to the presence of electronic states that can act as carrier traps and (iii) the large effective masses of both charge carriers. These limitations may be overcome by tailored nanostructuring as all the materials present anisotropic conductivity (according to the evaluation of carrier effective masses). In addition, doping these materials to increase conductivity could be a good strategy to achieve higher photocurrents and lower recombination rates. In a more general vein, we believe that this study illustrates how a combination of theoretical and experimental results may help advance toward the development of materials useful in the context of artificial photosynthesis.

Author contributions

A. C.: data curation, formal analysis, investigation, methodology, visualization, software, writing – original draft; F. J. P.: software, conceptualization, data curation, formal analysis, methodology, resources, supervision, writing – review & editing; A. P.-P.: data curation, formal analysis, methodology, supervision, writing – review & editing; N. V.: data curation, writing – review & editing; N. G.: methodology, writing – review & editing; T. L.-V.: writing – review & editing, funding acquisition; R. G.: conceptualization, data curation, funding acquisition, methodology, project administration, resources, supervision, validation, writing – review & editing.

Conflicts of interest

The authors declare that they have no known competing financial interests or personal relationships that could have appeared to influence the work reported in this paper.

Data availability

The data supporting this article have been included as part of the supplementary information (SI). Supplementary information: procedures for materials preparation, further photoelectrochemical characterization, DFT computational details and results (theoretical band edge energies), additional SEM images, flat band potentials, and comparison with literature. See DOI: https://doi.org/10.1039/d5ta08157b.

Acknowledgements

These results are part of the project TED2021-132697B-I00, funded by MCIN/AEI/10.13039/501100011033 and by the Union Europea "NextGenerationEU"/PRTR. We are also grateful to the MCINN/AEI/FEDER for financial support through projects PID2021-128876OB-I00 and PID2024-162784OB-I00. A. P.-P. and N. C. V are grateful to the Ministry of Universities, the European Union "NextGenerationEU" and the University of Alicante for the María Zambrano Fellowship. N. G. thanks the Spanish Ministry of Science & Innovation for the "Ramon y Cajal" Program (RYC2018-023888-I) funded by MCIN/AEI/10.13039/501100011033.

References

1 K. Sivula and R. van de Krol, *Nat. Rev. Mater.*, 2016, **1**, 15010.
2 K. Sivula, *Chimia*, 2013, **67**, 155.
3 A. Radmilovic, T. J. Smart, Y. Ping and K.-S. Choi, *Chem. Mater.*, 2020, **32**, 3262–3270.
4 T. T. Nguyen, M. Patel, S. Kim, V.-A. Dao and J. Kim, *ACS Appl. Mater. Interfaces*, 2021, **13**, 10181–10190.
5 T. Higashi, Y. Sasaki, Y. Kawase, H. Nishiyama, M. Katayama, K. Takanabe and K. Domen, *Catalysts*, 2021, **11**, 584.
6 C. Ros, T. Andreu and J. R. Morante, *J. Mater. Chem. A*, 2020, **8**, 10625–10669.
7 R.-T. Gao, J. Zhang, T. Nakajima, J. He, X. Liu, X. Zhang, L. Wang and L. Wu, *Nat. Commun.*, 2023, **14**, 2640.
8 A. K. Díaz-García and R. Gómez, *J. Photochem. Photobiol., A*, 2018, **366**, 65–71.
9 Z. Li, L. Luo, M. Li, W. Chen, Y. Liu, J. Yang, S.-M. Xu, H. Zhou, L. Ma, M. Xu, X. Kong and H. Duan, *Nat. Commun.*, 2021, **12**, 6698.
10 K. Hidayatullah, J. Manopo, I. Supu, A. Hadju, C. Ofiyen, M. K. Mahardhika and Y. Darma, *Inorg. Chem. Commun.*, 2025, **179**, 114885.
11 Y. Wang, X. Li and Y. Yang, *RSC Adv.*, 2022, **12**, 26099–26105.
12 Y. Li, Q. Mei, Z. Liu, X. Hu, Z. Zhou, J. Huang, B. Bai, H. Liu, F. Ding and Q. Wang, *Appl. Catal., B*, 2022, **304**, 120995.
13 X. Feng, Y. Chen, Z. Qin, M. Wang and L. Guo, *ACS Appl. Mater. Interfaces*, 2016, **8**, 18089–18096.
14 S. Ye, C. Ding, M. Liu, A. Wang, Q. Huang and C. Li, *Adv. Mater.*, 2019, **31**, 1902069.
15 S. A. Alves, L. L. Soares, L. A. Goulart and L. H. Mascaro, *J. Solid State Electrochem.*, 2016, **20**, 2461–2470.
16 W. A. Smith, I. D. Sharp, N. C. Strandwitz and J. Bisquert, *Energy Environ. Sci.*, 2015, **8**, 2851–2862.
17 X. WANG, W. qing QIN, F. JIAO, L. yang DONG, J. gen GUO, J. ZHANG and C. ren YANG, *Trans. Nonferrous Met. Soc. China*, 2022, **32**, 2318–2338.

18 S. Speldrich, M. Wark and G. Wittstock, *ACS Appl. Energy Mater.*, 2023, **6**, 9602–9614.
19 J. Cen, Q. Wu, D. Yan, W. Zhang, Y. Zhao, X. Tong, M. Liu and A. Orlov, *RSC Adv.*, 2019, **9**, 899–905.
20 Q. Yi, H. Wang and J.-M. Lee, *ChemElectroChem*, 2025, **12**, e202400600.
21 H. Abdullah, H. Shuwanto, J. Lie and M. Sillanpää, *J. Environ. Chem. Eng.*, 2023, **11**, 109356.
22 J. U. Lee, J. H. Kim and J. S. Lee, *Catalysts*, 2023, **13**, 1408.
23 K. Ikeue and T. Ueno, *Mater. Lett.*, 2023, **348**, 134690.
24 J. Yang, C. Li and P. Diao, *Electrochim. Acta*, 2019, **308**, 195–205.
25 C. Loka, D. Gelija, S. V. P. Vattikuti and K.-S. Lee, *ACS Sustain. Chem. Eng.*, 2023, **11**, 11978–11990.
26 J. Li, S. Hu, S. Liu, S. Hou, L. Li and J. Huang, *Int. J. Hydrogen Energy*, 2024, **61**, 967–974.
27 D. Wang, P. Bassi, H. Qi, X. Zhao, Gurudayal, L. Wong, R. Xu, T. Sritharan and Z. Chen, *Materials*, 2016, **9**, 348.
28 P. Ostellari, S. Benedoue, D. Zamboni, A. Basagni, S. Silloni, E. Scattolin, M. Lorenzoni, R. Pilot, I. Fortunati, S. Lauciello, M. Wang, M. Prato, J. N. Ndi, F. Arcudi, L. Đorđević, G. Meneghesso, S. Gross, L. Franco, G. Rizzi, T. Gatti and F. Lamberti, *Adv. Mater. Interfaces*, 2025, **12**, e00610.
29 M. Zhou, Z. Liu, X. Li and Z. Liu, *Ind. Eng. Chem. Res.*, 2018, **57**, 6210–6217.
30 L. Fan, J. Sunarso, X. Zhang, X. Xiong, L. He, L. Luo, F. Wang, Z. Fan, C. Wu, D. Han, N. H. Wong, Y. Wang, G. Chen and W. Chen, *Int. J. Hydrogen Energy*, 2022, **47**, 20153–20165.
31 W. Ye, F. Chen, F. Zhao, N. Han and Y. Li, *ACS Appl. Mater. Interfaces*, 2016, **8**, 9211–9217.
32 X. Xiong, L. Fan, G. Chen, Y. Wang, C. Wu, D. Chen, Y. Lin, T. Li, S. Fu and S. Ren, *Electrochim. Acta*, 2019, **328**, 135125.
33 J. U. Lee, J. H. Kim, K. Kang, Y. S. Shin, J. Y. Kim, J. H. Kim and J. S. Lee, *Renewable Energy*, 2023, **203**, 779–787.
34 C. Li, B. Guo, B. Peng, C. Yue and P. Diao, *Int. J. Electrochem. Sci.*, 2019, **14**, 9017–9029.
35 N. Nasori, D. Cao, Z. Wang, U. Farahdina, A. Rubiyanto and Y. Lei, *Molecules*, 2021, **26**, 2900.
36 X. M. C. Ta, T. K. A. Nguyen, A. D. Bui, H. T. Nguyen, R. Daiyan, R. Amal, T. Tran-Phu and A. Tricoli, *Adv. Mater. Technol.*, 2023, **8**, 2201760.
37 W. Qiu, Y. Zhang, G. He, L. Chen, K. Wang, Q. Wang, W. Li, Y. Liu and J. Li, *ACS Appl. Energy Mater.*, 2022, **5**, 11732–11739.
38 A. E. B. Lima, M. Assis, A. L. S. Resende, H. L. S. Santos, L. H. Mascaro, E. Longo, R. S. Santos, L. S. Cavalcante and G. E. Luz, *J. Solid State Electrochem.*, 2022, **26**, 997–1011.
39 P. Chatterjee and A. K. Chakraborty, *Sol. Energy*, 2022, **232**, 312–319.
40 F. Zhan, H. Zhao, G. Wen, Z. Ma, Y. Liu, M. Zhu, Y. Zheng, D. Chen and P. La, *New J. Chem.*, 2023, **47**, 1620–1624.
41 N. Doudin, S. Pomp, M. Blatnik, R. Resel, M. Vorokhta, J. Goniakowski, C. Noguera, F. P. Netzer and S. Surnev, *Surf. Sci.*, 2017, **659**, 20–30.
42 S. Shepard and M. Smeu, *Comput. Mater. Sci.*, 2018, **143**, 301–307.
43 E. Bandiello, P. Rodríguez-Hernández, A. Muñoz, M. B. Buenestado, C. Popescu and D. Errandonea, *Mater. Adv.*, 2021, **2**, 5955–5966.
44 B. Huang and J. N. Hart, *Phys. Chem. Chem. Phys.*, 2020, **22**, 1727–1737.
45 S. Dey, R. A. Ricciardo, H. L. Cuthbert and P. M. Woodward, *Inorg. Chem.*, 2014, **53**, 4394–4399.
46 J. P. Perdew, K. Burke and M. Ernzerhof, *Phys. Rev. Lett.*, 1996, **77**, 3865–3868.
47 C. M. Tian, M. Jiang, D. Tang, L. Qiao, H. Y. Xiao, F. E. Oropeza, J. P. Hofmann, E. J. M. Hensen, A. Tadich, W. Li, D. C. Qi and K. H. L. Zhang, *J. Mater. Chem. A*, 2019, **7**, 11895–11907.
48 D. Peeters, O. Mendoza Reyes, L. Mai, A. Sadlo, S. Cwik, D. Rogalla, H.-W. Becker, H. M. Schütz, J. Hirst, S. Müller, D. Friedrich, D. Mitoraj, M. Nagli, M. C. Toroker, R. Eichberger, R. Beranek and A. Devi, *J. Mater. Chem. A*, 2018, **6**, 10206–10216.
49 C. Kim, D. Jeon, N. Kim, J. Ryu and J. H. Lee, *Small*, 2024, 2400114.
50 G. Kresse and J. Furthmüller, *Phys. Rev. B:Condens. Matter Mater. Phys.*, 1996, **54**, 11169–11186.
51 P. E. Blöchl, *Phys. Rev. B:Condens. Matter Mater. Phys.*, 1994, **50**, 17953–17979.
52 G. Kresse and D. Joubert, *Phys. Rev. B:Condens. Matter Mater. Phys.*, 1999, **59**, 1758–1775.
53 S. L. Dudarev, G. A. Botton, S. Y. Savrasov, C. J. Humphreys and A. P. Sutton, *Phys. Rev. B:Condens. Matter Mater. Phys.*, 1998, **57**, 1505–1509.
54 F. J. Pastor, M. Contreras, T. Lana-Villarreal, J. M. Orts and R. Gómez, *Ceram. Int.*, 2023, **49**, 24812–24823.
55 A. Kalinko, A. Kuzmin, P. Roy and R. A. Evarestov, *Low Temp. Phys.*, 2016, **42**, 552–555.
56 J. B. Forsyth, C. Wilkinson and A. I. Zvyagin, *J. Phys.: Condens. Matter*, 1991, **3**, 8433.
57 S. Shanmugapriya, V. D. Nithya, A. Rajalakshmi, K. S. Sivaranjani, P. Bharathi, S. Shalini, P. R. Kasturi and R. K. Selvan, *J. Mater. Sci.: Mater. Electron.*, 2020, **31**, 15616–15626.
58 A. Maignan, M. Schmidt, Y. Prots, O. I. Lebedev, R. Daou, C.-F. Chang, C.-Y. Kuo, Z. Hu, C.-T. Chen, S.-C. Weng, S. G. Altendorf, L.-H. Tjeng and Y. Grin, *Chem. Mater.*, 2022, **34**, 789–797.
59 J. Mao, J. Zhao, L. Li, T. Chen, Q. Lv and Y. Li, *Chin. J. Phys.*, 2020, **63**, 163–167.
60 M. Jeyakanthan, U. Subramanian, R. B. Tangsali and A. Ramesh, *Phys. B*, 2020, **586**, 412151.
61 A. Jain, G. Hautier, C. J. Moore, S. Ping Ong, C. C. Fischer, T. Mueller, K. A. Persson and G. Ceder, *Comput. Mater. Sci.*, 2011, **50**, 2295–2310.
62 A. K. Mohamedkhair, Q. A. Drmosh, M. Qamar and Z. H. Yamani, *Catalysts*, 2021, **11**, 381.
63 S. Rajagopal, D. Nataraj, O. Yu. Khyzhun, Y. Djaoued, J. Robichaud and D. Mangalaraj, *J. Alloys Compd.*, 2010, **493**, 340–345.

64 S. G. Altendorf, D. Takegami, A. Meléndez-Sans, C. F. Chang, M. Yoshimura, K. D. Tsuei, A. Tanaka, M. Schmidt and L. H. Tjeng, *Phys. Rev. B*, 2023, **108**, 85119.
65 O. Y. Khyzhun, V. L. Bekenev, V. V Atuchin, E. N. Galashov and V. N. Shlegel, *Mater. Chem. Phys.*, 2013, **140**, 588–595.
66 G. Bakradze, A. Kalinko and A. Kuzmin, *J. Phys. Chem. Solids*, 2022, **161**, 110425.
67 V.-A. Ha, F. Ricci, G.-M. Rignanese and G. Hautier, *J. Mater. Chem. C*, 2017, **5**, 5772–5779.
68 L. Chen, W. Li, W. Qiu, G. He, K. Wang, Y. Liu, Q. Wu and J. Li, *ACS Appl. Mater. Interfaces*, 2022, **14**, 47737–47746.
69 M. Xiao, B. Luo, Z. Wang, S. Wang and L. Wang, *Sol. RRL*, 2020, **4**, 1900509.
70 J. H. Lopes, O. M. V. M. Bueno, I. O. Mazali and C. A. Bertran, *Mater. Sci. Eng., C*, 2019, **97**, 669–678.
71 M. Jeyakanthan, U. Subramanian and R. B. Tangsali, *J. Mater. Sci.: Mater. Electron.*, 2018, **29**, 1914–1924.
72 H. Harshan, K. P. Priyanka, A. Sreedevi, A. Jose and T. Varghese, *Eur. Phys. J. B*, 2018, **91**, 287.
73 K. Karoui, A. Ben Rhaiem and F. Jemni, *Ionics*, 2021, **27**, 1511–1524.
74 B. Iandolo, H. Zhang, B. Wickman, I. Zorić, G. Conibeer and A. Hellman, *RSC Adv.*, 2015, **5**, 61021–61030.
75 Y. Zhang, X. Chen, F. Jiang, Y. Bu and J.-P. Ao, *ACS Sustain. Chem. Eng.*, 2020, **8**, 9184–9194.
76 T. Li, J. He, B. Peña and C. P. Berlinguette, *Angew. Chem., Int. Ed.*, 2016, **55**, 1769–1772.
77 D. Liu, X. Chen, Y. Qiao, Y. Zhou and Y. Kuang, *Adv. Energy Sustainability Res.*, 2022, **3**, 2100146.
78 Y. Liu, L. Chen, X. Zhu, H. Qiu, K. Wang, W. Li, S. Cao, T. Zhang, Y. Cai, Q. Wu and J. Li, *J. Electroanal. Chem.*, 2022, **924**, 116859.
79 A. Venugopal and W. A. Smith, *Faraday Discuss.*, 2019, **215**, 175–191.
80 C. A. Mesa, A. Kafizas, L. Francàs, S. R. Pendlebury, E. Pastor, Y. Ma, F. Le Formal, M. T. Mayer, M. Grätzel and J. R. Durrant, *J. Am. Chem. Soc.*, 2017, **139**, 11537–11543.
81 K. Wang, L. Chen, X. Liu, J. Li, Y. Liu, M. Liu, X. Qiu and W. Li, *Chem. Eng. J.*, 2023, **471**, 144730.
82 J. Li, S. K. Cushing, P. Zheng, F. Meng, D. Chu and N. Wu, *Nat. Commun.*, 2013, **4**, 2651.
83 X. Zhong, H. He, M. Yang, G. Ke, Z. Zhao, F. Dong, B. Wang, Y. Chen, X. Shi and Y. Zhou, *J. Mater. Chem. A*, 2018, **6**, 10456–10465.
84 D. Tafalla, P. Salvador and R. M. Benito, *J. Electrochem. Soc.*, 1990, **137**, 1810.
85 B. Liu, S. Wang, G. Zhang, Z. Gong, B. Wu, T. Wang and J. Gong, *Chem. Soc. Rev.*, 2023, **52**, 4644–4671.
86 A. Cots, P. Bonete, D. Sebastián, V. Baglio, A. S. Aricò and R. Gómez, *ACS Appl. Mater. Interfaces*, 2018, **10**, 25393–25400.